ADVANCED MATERIALS
www.advmat.de

Iridium Single-Atom-Ensembles Stabilized on Mn-Substituted Spinel Oxide for Durable Acidic Water Electrolysis

*Ashwani Kumar, Marcos Gil-Sepulcre, Jinsun Lee, Viet Q. Bui, Yue Wang, Olaf Rüdiger, Min Gyu Kim, Serena DeBeer, and Harun Tüysüz**

Exploring single-atom-catalysts for the acidic oxygen evolution reaction (OER) is of paramount importance for cost-effective hydrogen production via acidic water electrolyzers. However, the limited durability of most single-atom-catalysts and Ir/Ru-based oxides under harsh acidic OER conditions, primarily attributed to excessive lattice oxygen participation resulting in metal-leaching and structural collapse, hinders their practical application. Herein, an innovative strategy is developed to fabricate short-range Ir single-atom-ensembles (Ir_{SAE}) stabilized on the surface of Mn-substituted spinel Co_3O_4 (Ir_{SAE}-CMO), which exhibits excellent mass activity and significantly improved durability (degradation-rate: ≈2 mV h^{-1}), outperforming benchmark IrO_2 (≈44 mV h^{-1}) and conventional $Ir_{single\text{-}atoms}$ on pristine-Co_3O_4 for acidic OER. First-principle calculations reveal that Mn-substitution in the octahedral sites of Co_3O_4 substantially reduces the migration energy barrier for $Ir_{single\text{-}atoms}$ on the CMO surface compared to pristine-Co_3O_4, facilitating the migration of $Ir_{single\text{-}atoms}$ to form strongly correlated Ir_{SAE} during pyrolysis. Extensive ex situ characterization, operando X-ray absorption and Raman spectroscopies, pH-dependence activity tests, and theoretical calculations indicate that the rigid Ir_{SAE} with appropriate Ir–Ir distance stabilized on the CMO surface effectively suppresses lattice oxygen participation while promoting direct O—O radical coupling, thereby mitigating Ir-dissolution and structural collapse, boosting the stability in an acidic environment.

1. Introduction

Water electrolysis driven by renewable electricity for green hydrogen fuel production has gained significant recognition as a promising and sustainable technology.[1,2] Compared to conventional alkaline water electrolyzers, proton exchange membrane water electrolyzers operating in acidic media offer numerous key advantages, including high energy efficiency, current density, and hydrogen purity.[3,4] Nevertheless, the practical implementation of acidic water electrolyzers faces significant obstacles primarily due to the scarcity of affordable, active, and durable electrocatalysts for the acidic oxygen evolution reaction (OER).[5] Most of the reported OER electrocatalysts (e.g., spinel Co_3O_4,[6] Ni–Fe-oxide/alloy,[7,8] and metal-hydroxide/nitride[9,10]) have demonstrated excellent performance in alkaline environments. However, their effectiveness and stability are notably hampered by sluggish reaction kinetics in acids and severe degradation when exposed to strong acidic and oxidative conditions.[5,11] Hence, developing active and stable acidic OER electrocatalysts under these conditions remains a major challenge.

Currently, precious metals such as ruthenium/iridium-based oxides with reasonable activities are commonly utilized as OER electrocatalysts in acidic water electrolyzers. However, the high cost and limited availability of these metals severely limit their widespread use.[12] Moreover, both IrO_2 and RuO_2 exhibit

A. Kumar, J. Lee, Y. Wang, H. Tüysüz
Max-Planck-Institut für Kohlenforschung
45470 Mülheim an der Ruhr, Germany
E-mail: tueysuez@kofo.mpg.de, harun.tuysuz@imdea.org
M. Gil-Sepulcre, O. Rüdiger, S. DeBeer
Max Planck Institute for Chemical Energy Conversion
Stiftstrasse 34–36, D-45470 Mülheim an der Ruhr, Germany
The ORCID identification number(s) for the author(s) of this article can be found under https://doi.org/10.1002/adma.202401648

DOI: 10.1002/adma.202401648

V. Q. Bui
Advanced Institute of Science and Technology
The University of Danang
41 Le Duan, Danang 550000, Vietnam
M. G. Kim
Beamline Research Division
Pohang Accelerator Laboratory (PAL)
Pohang 790-784, South Korea
H. Tüysüz
IMDEA Materials Institute
Calle Eric Kandel 2, Getafe, Madrid 28906, Spain

insufficient durability in acidic OER, primarily due to the involvement of lattice oxygen through the lattice oxygen-mediated mechanism (LOM; direct O–$O_{Lattice}$ coupling between the oxo-radical and lattice oxygen) rather than the conventional adsorbate evolution mechanism (AEM).[3,13] Consequently, the LOM pathway in the acidic environment leads to the cleavage of metal-$O_{lattice}$ bonds and intensifies the collapse of the crystal structure, resulting in the metal dissolution, leading to deactivation under harsh acidic and oxidative conditions.[14] To mitigate costs and strike a balance between activity and durability in acidic OER, various strategies such as alloying,[15] mixed-metal oxides,[16] doping,[17] morphology tuning,[18] and defect engineering,[19] have been employed. Such strategies aim to promote the adsorbate evolution mechanism (*OOH formation) or oxide path mechanism (OPM; direct oxo–oxo radical coupling) while impeding excessive participation of lattice oxygen via the LOM pathway. Nevertheless, achieving a satisfactory balance between low cost and high performance (activity/stability) in acidic conditions remains challenging.

Recently, single-atom catalysts (SACs) with ultimate atom economy, unique electronic properties, and reduced usage of noble-metal have attracted significant attention for various applications, including electrocatalytic OER.[20–22] The low-cost transition metal oxides have emerged as highly effective support materials for stabilizing active single atoms in electrocatalytic water splitting, particularly in acidic water oxidation reactions.[3,18,21] However, the weak single-atom-support interaction and absence of strong atomic spatial correlation (arrangement of nearest single-atom neighbors on oxide-support), makes the single-atom-$O_{support}$ bonds highly susceptible to corrosion/dissolution due to enhanced lattice oxygen participation, resulting in severe deactivation under harsh acidic OER conditions.[23,24] Therefore, there is an urgent need to develop effective strategies for manipulating the active single-atom-support coordination environment and optimizing their short-range spatial correlation by precisely tuning the surface energy of the oxide support. Such approaches could promote the adsorbate evolution mechanism or oxide path mechanism, while concurrently suppressing lattice oxygen participation, ultimately improving durability in acidic OER.

In light of the preceding discussion, we present a straightforward strategy for modulating the surface energy of spinel Co_3O_4 support via Mn-substitution (Co_2MnO_4: CMO), enabling precise stabilization of spatially correlated Ir single-atom-ensembles (Ir_{SAE}-CMO), which can efficiently catalyze the sluggish acidic OER under harsh oxidative environment. Theoretical calculations reveal that Mn-substitution in the octahedral sites of Co_3O_4 significantly alters the surface binding energy and reduces the migration energy barrier for isolated $Ir_{single\text{-}atoms}$ (Ir_{SA}) on the CMO surface compared to pristine-Co_3O_4, facilitating the migration of Ir_{SA} to form strongly correlated Ir_{SAE} during the pyrolysis process. The as-prepared Ir_{SAE}-CMO exhibits remarkable catalytic OER performance, achieving high mass activity and much-improved durability compared to commercial IrO_2 and conventional Ir_{SA} on pristine-Co_3O_4. Holistic ex situ characterizations, operando Raman and X-ray absorption spectroscopy, pH-dependence activity tests, and theoretical studies collectively indicate that the strongly correlated Ir_{SAE} on the CMO support effectively suppresses lattice oxygen participation in acidic OER. Simultaneously, the short interatomic Ir-Ir distance within Ir_{SAE} facilitates direct O—O radical coupling, thereby mitigating Ir-dissolution and crystal structural collapse, boosting the durability in the acidic OER environment.

2. Results and Discussion

2.1. Synthesis and Structural Characterization

The synthesis strategy for stabilizing short-range spatially correlated Ir_{SAE} on Mn-substituted spinel Co_3O_4 and isolated Ir_{SA} on pristine Co_3O_4 surfaces could be divided into four steps, as schematically illustrated in Figure S1 (Supporting Information). First, Co-hydroxide and Mn-substituted Co-hydroxide precursors were electrodeposited directly onto a conductive carbon cloth (CC), followed by calcination at 350 °C for 3 h to obtain pristine-Co_3O_4 and Mn-substituted spinel (Co_2MnO_4: CMO), respectively, with pure face-centered cubic (fcc) phase (JCPDS: 74–1657), confirmed by the X-ray diffraction (XRD) patterns (**Figure 1a**).[21,25] Compared to Co_3O_4, the downshifted (311) diffraction peak of CMO with Co:Mn ratio of 2:1, revealed by the energy dispersive X-ray spectroscopy (EDS) analysis, suggested the incorporation of Mn into the lattice of spinel Co_3O_4 (Figures S2a and S3a, Supporting Information).[8] No additional impurity phases (such as Mn_2O_3) were detected in the high-resolution XRD pattern of CMO, suggesting the successful synthesis of pure CMO spinel structure (Figure S2b, Supporting Information). The field-emission scanning electron microscopy (FE-SEM) images further revealed uniform plate-like morphologies of Co_3O_4 and CMO with highly rough surfaces (Figure S4a,b, Supporting Information).

Subsequently, the Co_3O_4 and CMO supports were immersed in an ethanolic Ir ion solution (6 mg mL^{-1}) for 30 min, followed by annealing in air at 350 °C for 2 h to form isolated Ir_{SA} on the Co_3O_4 (Ir_{SA}-Co_3O_4) and short-range Ir_{SAE} on the CMO (Ir_{SAE}-CMO) surface. The crystal phase and morphologies of Ir_{SA}-Co_3O_4 and Ir_{SAE}-CMO were similar to those of their respective substrates, further confirming the absence of any Ir-based nanoparticles (Figure 1a; Figures S2 and S4c,d, Supporting Information). Inductively coupled plasma optical emission spectrometry (ICP-OES) and EDS results further confirmed a high Ir loading of 9.2 and 9.5 wt% on the surfaces of Co_3O_4 and CMO, respectively (Figure S3b,c and Table S1, Supporting Information). The aberration-corrected high-angle annular dark-field scanning transmission electron microscopy (HADDF-STEM) image with a sub-Å resolution of Ir_{SA}-Co_3O_4 clearly demonstrated the existence of isolated bright spots marked by orange circles on the Co_3O_4 surface, proving direct and visual evidence for the stabilization of isolated Ir_{SA} sites (Figure S5a,b and S6a, Supporting Information).[26] Moreover, the existence and uniform distribution of isolated Ir_{SA} on the Co_3O_4 surface were further corroborated by the intensity profiles and corresponding EDS elemental mapping (Figure S6b–d, Supporting Information). Conversely, the HAADF-STEM images of Ir_{SAE}-CMO demonstrated the formation of short-range spatially correlated Ir_{SA}-ensembles, along with a few isolated Ir_{SA} sites on the CMO surface, indicating that Mn-substitution in the Co_3O_4 lattice facilitated the migration of Ir_{SA} to form short-range Ir_{SAE} during the pyrolysis process (Figure 1b; Figure S5c,d, Supporting Information). The distribution graph presented in Figure 1b (bottom image) accurately

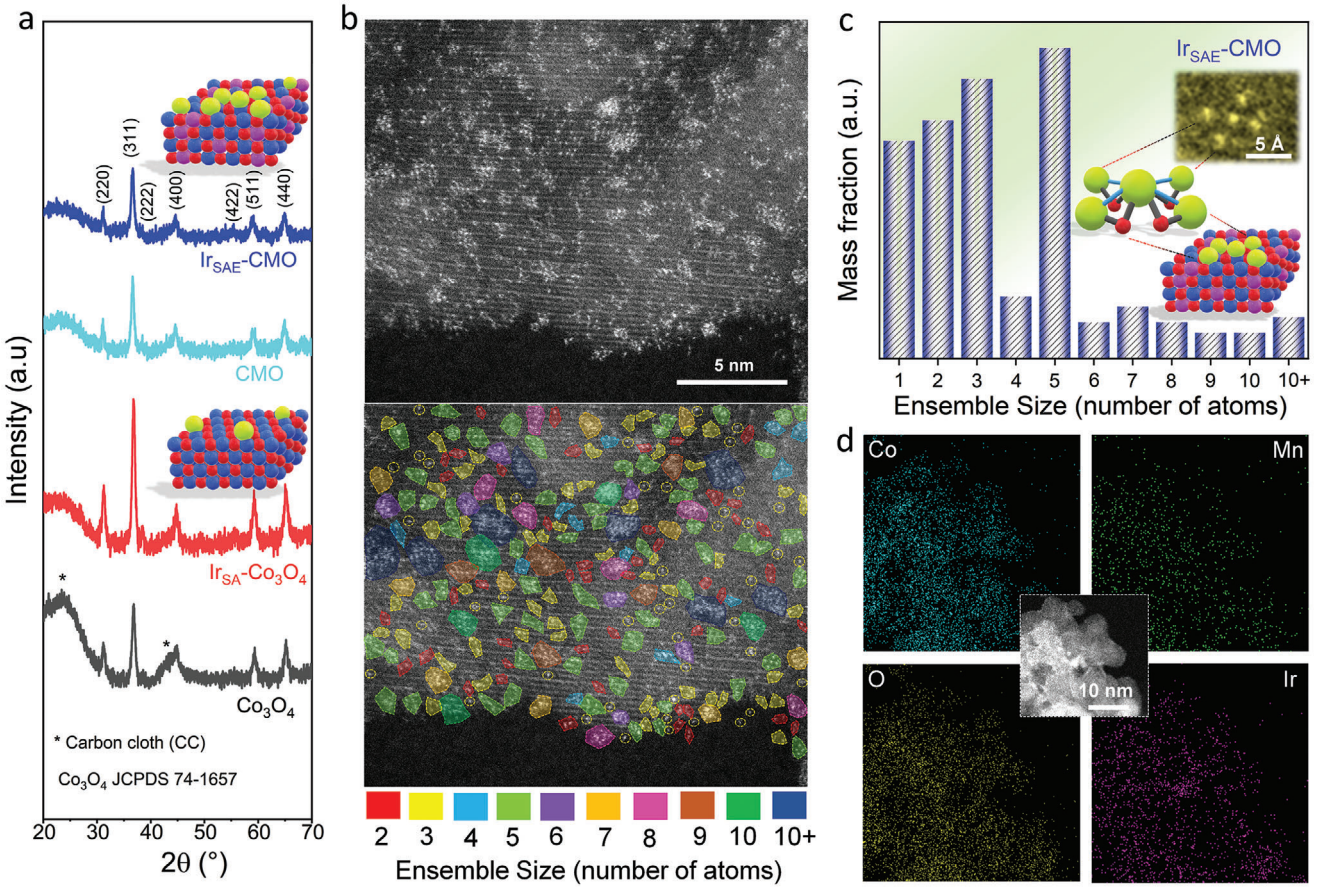

Figure 1. Structural characterizations and electron microscopy. a) XRD patterns of Co_3O_4, Ir_{SA}-Co_3O_4, CMO, and Ir_{SAE}-CMO. b) Upper: Aberration-corrected HAADF-STEM image of the Ir_{SAE}-CMO with bright spots corresponding to the Ir sites stabilized on the CMO surface; lower: Ir_{SAE} size distribution graph for short-range correlated Ir sites. c) Mass fraction histogram of the identified single-atom-ensembles in (b) (lower) with different numbers of short-range Ir sites. The inset shows the magnified AC-HAADF STEM image of an Ir_{SAE} site with five correlated Ir atoms and the corresponding proposed atomic model (Co: navy; Mn: purple; Ir: yellow and O: red). d) HAADF-STEM image and corresponding EDS maps of Ir_{SAE}-CMO showing the uniform dispersion of Ir (pink), Co (blue), Mn (green), and O (yellow).

depicted the labeling and classification of the projected Ir_{SAE} with short-range order observed on the CMO surface. Furthermore, the statistical analysis of the relative population of the projected Ir ensembles, determined based on mass fraction, indicated that a significant proportion of Ir sites exhibited a short-range Ir_{SAE} structure (mass fraction of Ir_{SAE}: ≈85% and mass fraction of Ir_{SA}: ≈15%) comprising five correlated Ir atoms within a close proximity (Figure 1c; Figure S7, Supporting Information). Meanwhile, the mass fraction of ensembles decreased with increasing ensemble size. The uniform distribution of Ir, Co, Mn, and O on Ir_{SAE}-CMO was revealed by HAADF-STEM and corresponding EDS elemental mapping (Figure 1d).

To further unveil the crucial role of Mn-substituted Co_3O_4 (CMO) surface facilitating the formation of short-range Ir_{SAE} rather than isolated Ir_{SA}, density functional theory (DFT) calculations were employed to investigate the migration energy barrier of Ir_{SA} as well as the binding strengths of Ir_{SA}/Ir_{SAE} on both the surfaces (Co_3O_4/CMO)[21]. Representative models, Ir_{SA}/Co_3O_4 for the pristine-Co_3O_4 surface and Ir_{SA}/CMO for the CMO surface were utilized to simulate the migration energies from the initial state to the final state (**Figure** 2a; Figure S8, Supporting Information). The migration energy barrier for Ir_{SA} on the CMO surface was found to be 0.91 eV, significantly lower than the observed value of 1.13 eV on the Co_3O_4 surface. This substantial decrease implies lower thermal stability and enhanced mobility of Ir_{SA} on the CMO surface compared to those on pristine-Co_3O_4, thus facilitating the migration of Ir_{SA} species and enabling the formation of spatially correlated Ir_{SAE} during the thermal treatment process. Additionally, the binding energy of Ir_{SAE} on the CMO surface (−6.20 eV) exhibited a more negative value compared to Ir_{SA} on CMO (−5.49 eV) and Ir_{SAE} on Co_3O_4 (−5.21 eV), indicating a significantly stronger affinity of Ir_{SAE} for the CMO surface (Figure 2b; Figure S9, Supporting Information). These interactions might be advantageous for enhancing corrosion resistance and impeding structural collapse under harsh acidic oxidative environments. Moreover, the strong electronic interaction between the rigid Ir_{SAE} and CMO support was further corroborated by the charge density difference analysis (Figure 2c), which revealed a significant charge redistribution and transfer from Ir_{SAE} to the adjacent CMO surface, resulting in highly electron-deficient Ir_{SAE} sites, which could be beneficial for accelerating the kinetics of oxidation reactions. Therefore, the DFT calculations clearly revealed

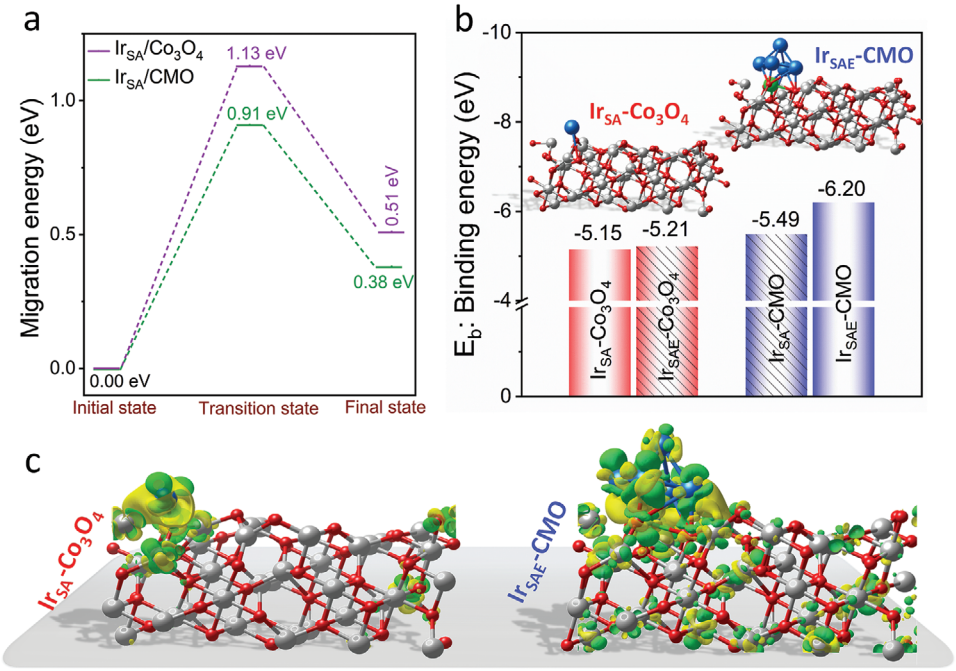

Figure 2. DFT calculations. a) Calculated migration energy barriers for Ir_{SA} on the surface of Co_3O_4 (purple line) and CMO (olive line) migrating from the initial to the final state. b) Comparison of the binding energies of Ir_{SA}/Ir_{SAE} on the surface of Co_3O_4 and CMO. Inset shows the corresponding atomic models of Ir_{SA}-Co_3O_4 and Ir_{SAE}-CMO. Color code: Ir (navy), Co (silver), Mn (green), and O (red). c) Charge density difference plot of Ir_{SA}-Co_3O_4 (left), and Ir_{SAE}-CMO (right). The yellow and green regions represent charge accumulation and charge depletion, respectively, with an isosurface value of 0.006 e^- $Å^{-3}$.

that replacing a Co^{3+} (octahedral site) with Mn significantly alters the surface energy of the support, thereby reducing the migration energy barrier for Ir_{SA} and promoting the formation of short-range Ir_{SAE} on the CMO support with considerably stronger affinity.

The electronic structure and local coordination environment of the Ir was investigated by X-ray absorption spectroscopy (XAS) and X-ray photoelectron spectroscopy (XPS) measurements. The rising edge of the Co K-edge X-ray absorption near-edge structure (XANES) spectra of Ir_{SAE}-CMO and CMO displayed a slightly negative shift in energy compared to pristine-Co_3O_4, consistent with a lower average oxidation state of Co atoms, which may be attributed to the substitution of Co^{3+} by Mn in the octahedral sites of spinel Co_3O_4 (Figure S10a, Supporting Information). Additionally, the Mn K-rising edge positions of Ir_{SAE}-CMO and CMO were located between those of Mn_3O_4 and MnO_2, indicating an average oxidation state of Mn around +3 and further supporting the substitution of octahedral Co^{3+} by Mn^{3+} in the Co_3O_4 spinel lattice (Figure S11a,b, Supporting Information). Compared to metallic Ir, the maximum of the Ir L_3-edge absorption spectra of Ir_{SAE}-CMO and Ir_{SA}-Co_3O_4 were shifted to higher energy values and located close to that of IrO_2, which results in an Ir oxidation state close to +4, consistent with the charge density difference analysis (**Figure 3a**). The Ir_{SAE}-CMO and Ir_{SA}-Co_3O_4 samples also displayed an increase in the intensity of the L_3-edge maximum compared to IrO_2, which indicates that these Ir centers are clearly different from that of pristine IrO_2 and suggest the presence of more d-hole character (inset of Figure 3a). The atomic coordination environment of Ir, Co, and Mn was further analyzed by the Fourier-transformed k^3-weighted extended X-ray absorption fine structure (FT-EXAFS) analysis. As displayed in the Co K-edge FT-EXAFS spectra (Figure S10b–d and Table S2, Supporting Information), the characteristic Co-O, Co-Co/Mn_{oct}, and Co-Co/Mn_{Td} peaks expected for Co_3O_4 and Co_2MnO_4 (CMO) were found at bond distances of ca. 1.9, 2.8 and 3.4 Å, respectively.[21] The lower intensity of the FT peak corresponding to the Co_{oct}-Co/Mn_{oct} bond at ca. 2.8 Å in CMO and Ir_{SAE}-CMO, compared to Co_3O_4 and Ir_{SA}-Co_3O_4, provides additional evidence supporting the substitution of Co^{3+} by Mn^{3+} in the octahedral sites of spinel Co_3O_4 lattice. This was further corroborated by the Mn K-edge FT-EXAFS spectra displaying Mn—O (1.9 and 2.3 Å) and Mn—Co/Mn (ca. 2.9 and 3.7 Å) bond distances expected for Co_2MnO_4 (Figure S11c,d and Table S2, Supporting Information).

The Ir L_3-edge FT-EXAFS spectra of Ir_{SAE}-CMO and Ir_{SA}-Co_3O_4 (Figure 3b) were different than IrO_2 displaying broader peaks that suggest a certain degree of deviation from the ideal *Oh* geometry of IrO_2, indicating a different nature of the Ir sites. Consequently, both spectra can be fitted following a simple IrO_2 model (Figure 3b) with a split first shell, which although obtained $\Delta R = 0.1$ Å for fitted distances are at the limit of the resolution ($\Delta R = \pi/2\Delta k$, 0.15 Å), fit better the experimental spectra in comparison to a single path first shell model (Figure S12, Tables S3 and S4, Supporting Information). The first shell was dominated by Ir—O peaks at an average distance of ca. 2.0 Å for Ir_{SA}-Co_3O_4 and Ir_{SAE}-CMO, similar to bond distances expected for IrO_2 (2.0 Å). The FT-EXAFS spectrum of Ir_{SAE}-CMO showed peaks corresponding to the scattering with neighboring Ir

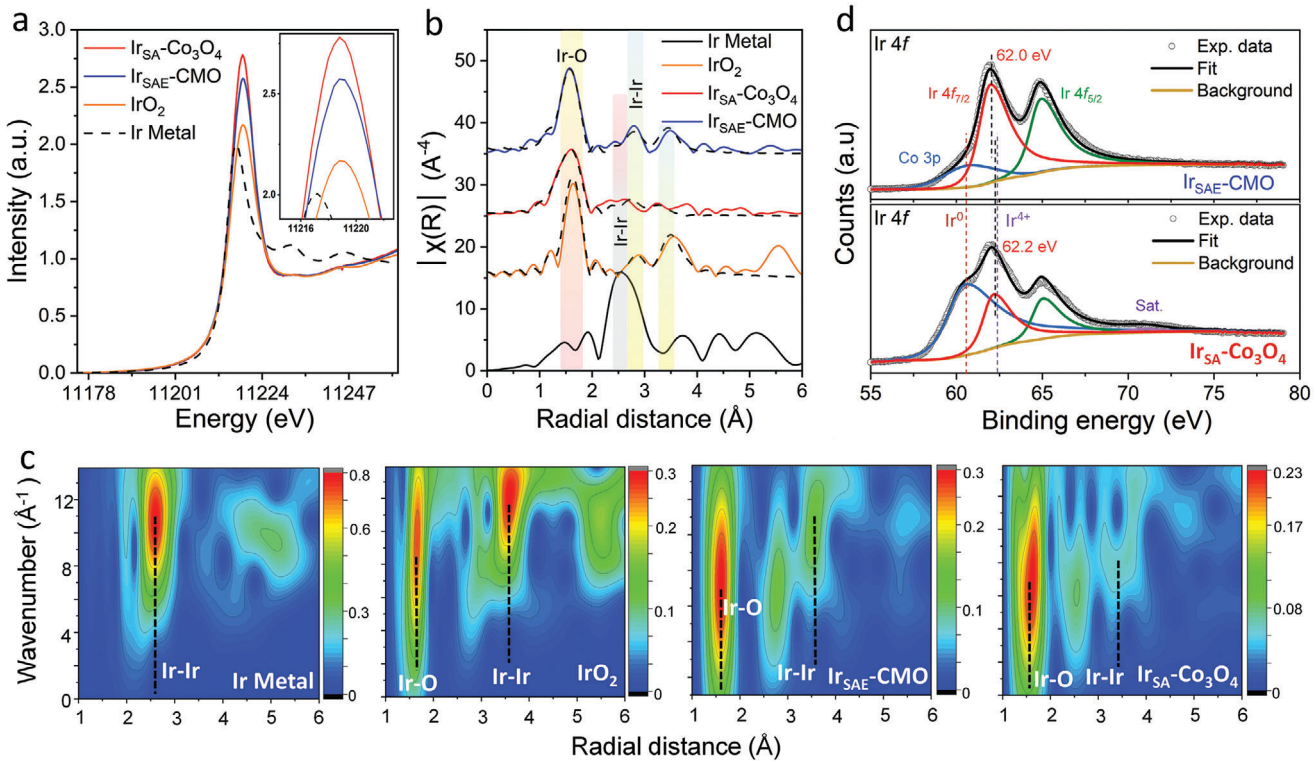

Figure 3. Electronic structure analysis. a) Experimental Ir-L_3 edge XANES spectra of Ir_{SAE}-CMO and Ir_{SA}-Co_3O_4 with other reference samples. The inset zooms in over the white line feature. b) Experimental (solid line) and fitted (dashed line) Ir-L_3 edge FT-EXAFS spectra of Ir_{SAE}-CMO and Ir_{SA}-Co_3O_4 with other reference samples. c) WT-EXAFS of Ir_{SAE}-CMO along with reference samples at Ir-L_3 edge. d) Fitted deconvoluted high-resolution Ir 4*f* XPS spectra of Ir_{SAE}-CMO and Ir_{SA}-Co_3O_4.

centers (Ir—O—Ir bond distances, similar to the features of IrO_2) suggesting the formation of Ir_{SAE}, whereas the Ir_{SA}-Co_3O_4 spectrum does not show those FT-EXAFS features, reflecting the isolated character of Ir single atomic species (Figure 3b). Furthermore, the presence of these Ir—O—Ir peaks at distances of 3.2 and 3.5 Å in the FT-EXAFS profile of Ir_{SAE}-CMO, were clearly shortened relative to the distances found for the second shell in IrO_2 (ca. 3.2 and 3.6 Å). This further supported the formation of Ir_{SAE} with assembled Ir sites on the CMO surface, in agreement with the magnified AC-HAADF STEM image and line-scanning intensity profile analysis of Ir_{SAE}-CMO. Moreover, the FT-EXAFS results were supported by the Ir L_3-edge wavelet transform-EXAFS analysis (Figure 3c), which further revealed the presence of Ir—O and an intense scattering between neighboring Ir in IrO_2, while the signal intensity related to the Ir–Ir of the second shell decrease in for Ir_{SAE}-CMO and Ir_{SA}-Co_3O_4, confirming the absence of aggregated IrO_2-based metallic nanoparticles.

The primary peak in the Co $2p_{3/2}$ XPS spectra of CMO and Ir_{SAE}-CMO exhibited a shift toward higher binding energy compared to Co_3O_4, consistent with the Co K-edge XANES results (Figure S13a, Supporting Information). Whereas, the Mn 2*p* XPS spectra of CMO and Ir_{SAE}-CMO indicated the presence of Mn^{3+}, collectively supporting the substitution of Co^{3+} by Mn^{3+} in the octahedral sites of spinel Co_3O_4 (Figure S13b, Supporting Information). The O 1*s* XPS spectra displayed negligible changes after the incorporation of Mn or stabilization of Ir_{SA}/Ir_{SAE} on the support surfaces (Figure S13c, Supporting Information). The Ir 4*f* XPS spectra of Ir_{SA}-Co_3O_4 and Ir_{SAE}-CMO demonstrated a partial positive oxidation state close to +4 for both Ir_{SA} and Ir_{SAE}, providing further confirmation of their highly electron deficient nature, in agreement with the Ir L_3-edge XANES and charge density difference analysis (Figure 3d). All the above results clearly point to the stabilization of an electron-deficient and rigid Ir_{SAE} on the CMO surface with short interatomic Ir–Ir distance, expected to enhance the activity and durability under challenging oxidative OER conditions.

2.2. Electrocatalytic Performance Toward Acidic Media OER

The electrocatalytic OER performances of the synthesized and commercial catalysts were evaluated in acidic media (0.5 M H_2SO_4) using a typical three-electrode setup.[27] The potential of the reference electrode was calibrated in an H_2 saturated electrolyte, and all the potentials were converted to the reversible hydrogen electrode (RHE) (Figure S14, Supporting Information).[20] As depicted in the *iR*-compensated linear sweep voltammetry (LSV) polarization curves in **Figure 4a,b**, the Ir_{SAE}-CMO exhibited remarkable acidic OER activity, requiring only 235 ± 8 and 345 ± 6 mV overpotential (η) to reach current densities of 10 and 100 mA cm^{-2}, respectively. This clearly outperforms the state-of-the-art IrO_2 (η_{10}: 290 mV and η_{100}: 430 mV), conventional Ir_{SA}-Co_3O_4 (η_{10}: 231 ± 4 mV and

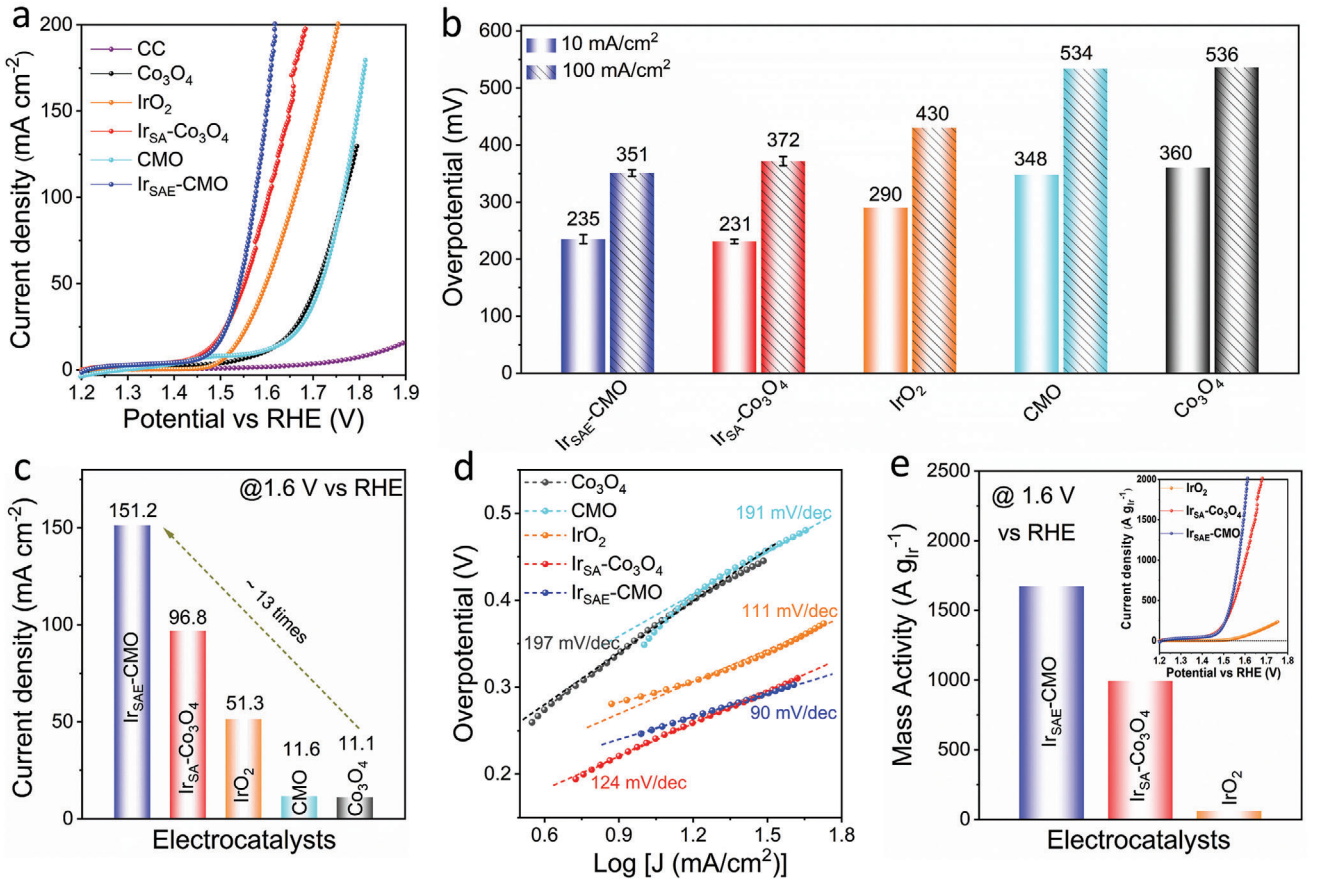

Figure 4. Electrochemical acidic OER performance. a–d) OER LSV polarization curves (iR-corrected) a), the overpotentials required to reach 10 and 100 mA cm^{-2} b), the current density reached at 1.6 V vs RHE c), and corresponding Tafel plots d), in 0.5 M H_2SO_4. e) Mass activity of Ir_{SAE}-CMO with Ir_{SA}-Co_3O_4 and IrO_2 in 0.5 M H_2SO_4 at 1.6 V vs RHE. The inset shows the noble-metal-mass normalized OER LSV polarization curves of Ir_{SAE}-CMO with Ir_{SA}-Co_3O_4 and IrO_2 in 0.5 M H_2SO_4.

η_{100}: 372 ± 8 mV), and other control samples (Figure S15, Supporting Information). Furthermore, the Ir_{SAE}-CMO delivered the highest current density at 1.6 V vs RHE among all the investigated samples, exhibiting a 13-fold increase compared to the bare Co_3O_4/CMO supports and demonstrating that the Ir_{SAE} is the primary contributor toward the superior acidic OER activity (Figure 4c). The Ir_{SAE}-CMO exhibited the lowest Tafel slope (90 mV dec^{-1}) compared to Ir_{SA}-Co_3O_4 (124 mV dec^{-1}) and IrO_2 (111 mV dec^{-1}), indicating a more favorable acidic OER kinetics (Figure 4d).

The Ir_{SAE}-CMO also demonstrated ultrahigh noble-metal-mass normalized acidic OER activity to that of IrO_2 and Ir_{SA}-Co_3O_4 at 1.6 V vs RHE, indicating that the Ir_{SAE} sites can effectively improve the performance compared to those of commercial IrO_2 with remarkable economic efficiency (Figure 4e). The superior acidic OER activity of the Ir_{SAE}-CMO was further corroborated by the smallest charge transfer resistance (R_{CT}) with a reasonably high electrochemically active surface area (ECSA), suggesting rapid electron transfer kinetics and a high abundance of active sites, contributing to enhanced OER performance (Figures S16 and S17, Supporting Information). Moreover, the ECSA-normalized acidic OER LSV polarization curve further confirmed the superior intrinsic activity of Ir_{SAE}-CMO compared to the conventional Ir_{SA}-Co_3O_4 (Figure S18, Supporting Information).

Apart from the superior activity, the durability of the catalyst is another essential figure-of-merit for real application, especially in acidic conditions. The long-term stability test was performed by chronopotentiometry analysis.[4,28] The Ir_{SAE}-CMO exhibited excellent long-term stability under acidic OER conditions for at least 25 h at 10 mA cm^{-2} with an ultralow degradation rate of ≈2 mV h^{-1} (retention: ≈96%) (**Figure 5a**). This rate is over 22 and 7 times slower than that of the commercial IrO_2 (≈44 mV h^{-1}) and conventional Ir_{SA}-Co_3O_4 (≈14 mV h), respectively. The overlapping LSV curves measured before and after the stability test further confirmed the retention of active sites and high catalytic activity of Ir_{SAE}-CMO, as comparison to Ir_{SA}-Co_3O_4 and IrO_2 (Figure S19, Supporting Information). To monitor the stability of the catalysts under acidic OER conditions, the dissolution of ions in the electrolyte during the electrolysis was measured using ICP-OES. The Ir_{SAE}-CMO displayed negligible leaching of Ir ions during the stability test, while a slight dissolution of surface Co/Mn ions was observed in the initial hours of OER, consistent with the previous reports that transition metal species underwent surface leaching in acidic OER conditions (Figure 5b).[29] In contrast,

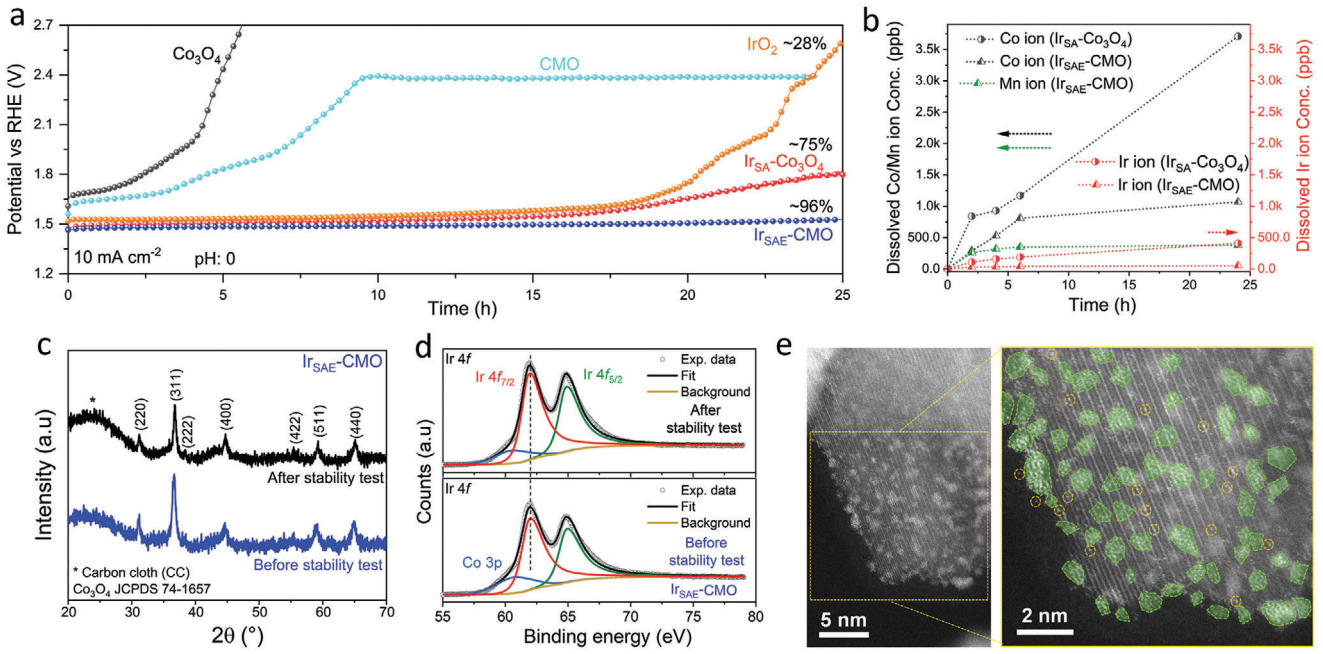

Figure 5. Stability test and post-stability characterizations. a) Chronopotentiometric stability test of Ir_{SAE}-CMO, Ir_{SA}-Co_3O_4, IrO_2, Co_3O_4, and CMO in 0.5 M H_2SO_4 at a current density of 10 mA cm^{-2}. b) Dissolved Co and Mn (left-*y*-axis) and Ir (right-*y*-axis) ions concentrations measured for Ir_{SAE}-CMO, and Ir_{SA}-Co_3O_4 in the electrolyte by ICP-OES. c,d) XRD pattern c), and high-resolution Ir 4*f* XPS spectra d), of Ir_{SAE}-CMO before and after the stability test. e) AC-HAADF STEM image of Ir_{SAE}-CMO after the stability test (orange circle: isolated Ir_{SA}; green patch: Ir_{SAE}).

Co_3O_4, CMO, and Ir_{SA}-Co_3O_4 suffered from severe leaching of Ir, Co, and Mn ions during the stability test (Figure 5b; Figure S20, Supporting Information). The post-stability characterizations (XRD, XPS, XAS, HAADF-STEM, FESEM, and EDS) of Ir_{SAE}-CMO revealed the well-preserved crystal structure, chemical states of Ir/Co/Mn, and the robust Ir_{SAE} structure after the durability test (Figure 5c–e; Figures S21 and S22 and Table S3, Supporting Information). More importantly, the post-stability HAADF-STEM, Ir 4*f* XPS, and Ir L_3-edge XAS analysis of Ir_{SAE}-CMO ruled out the formation of metallic Ir-nanoparticles after the acidic OER, indicating that the rigid Ir_{SAE} are strongly anchored to the CMO surface, maintaining their structural integrity and preventing migration during the stability tests. In addition, the Ir_{SAE}-CMO also exhibited a high energy-conversion efficiency (Faradaic efficiency) of ≈93 ± 1.5% for acidic OER, suggesting that charge is mainly consumed for OER without allied parasitic reactions (Figure S23, Supporting Information). The excellent acidic OER performance (activity/stability) of Ir_{SAE}-CMO was comparable and better than many of the recently reported acidic OER electrocatalysts (Figure S24 and Table S5, Supporting Information).

2.3. Mechanistic Investigations

To gain further insights into the origin of high performance and acidic OER mechanism of Ir_{SAE}-CMO, we employed in situ Raman spectroscopy, operando X-ray absorption spectroscopy, pH-dependent electrocatalytic activity measurements, and molecular probe to diagnose specific intermediate generated during OER. in situ Raman measurement conducted during OER (**Figure 6a**; Figure S25, Supporting Information) revealed that all the characteristic bands (A_{1g} at ≈695 cm^{-1}, F_{2g} at ≈530 and 601 cm^{-1}, and E_g at ≈480 cm^{-1}, originated from Mn-substituted spinel Co_3O_4) of Ir_{SAE}-CMO remained intact. This indicates the absence of significant surface phase evolution throughout the entire OER process, highlighting the excellent structural stability of Ir_{SAE}-CMO under acidic conditions. In general, electrocatalytic OER on metal oxide surfaces might follow two different mechanisms, i.e., conventional adsorbate evolution mechanism (AEM) involving multiple intermediates (*OH, *O, and *OOH) and lattice oxygen-mediated mechanism (LOM) bypassing *OOH intermediate (involving lattice oxygen participation), leading to faster kinetics compared to AEM.[30] However, LOM in acidic media intensifies the metal-$O_{lattice}$ bond cleavage and crystal structure collapse, resulting in severe metal dissolution and poor stability.[13]. More recently, oxide path mechanism (OPM) involving fewer intermediates (*O and *OH) has been proposed to exhibit similar or faster OER kinetics than LOM, allowing direct O—O radical coupling to generate molecular oxygen without sacrificing stability, while avoiding the participation of lattice oxygen.[31] Nevertheless, the oxide path mechanism has stringent requirements for the geometric configuration of metal active sites with appropriate interatomic distance to promote direct O-O radical coupling.

To investigate lattice oxygen participation in the OER process, we performed pH-dependent LSV measurements for Ir_{SAE}-CMO and Ir_{SA}-Co_3O_4. The pH-dependent activity, reflective of the proton transfer decoupled from the electron transfer process, provides insights into the LOM-mediated OER process involving lattice oxygen participation, refilling of the generated oxygen vacancies via H_2O/OH^- ions from electrolyte and the subsequent chemical deprotonation step.[32] As revealed in Figure 6b and

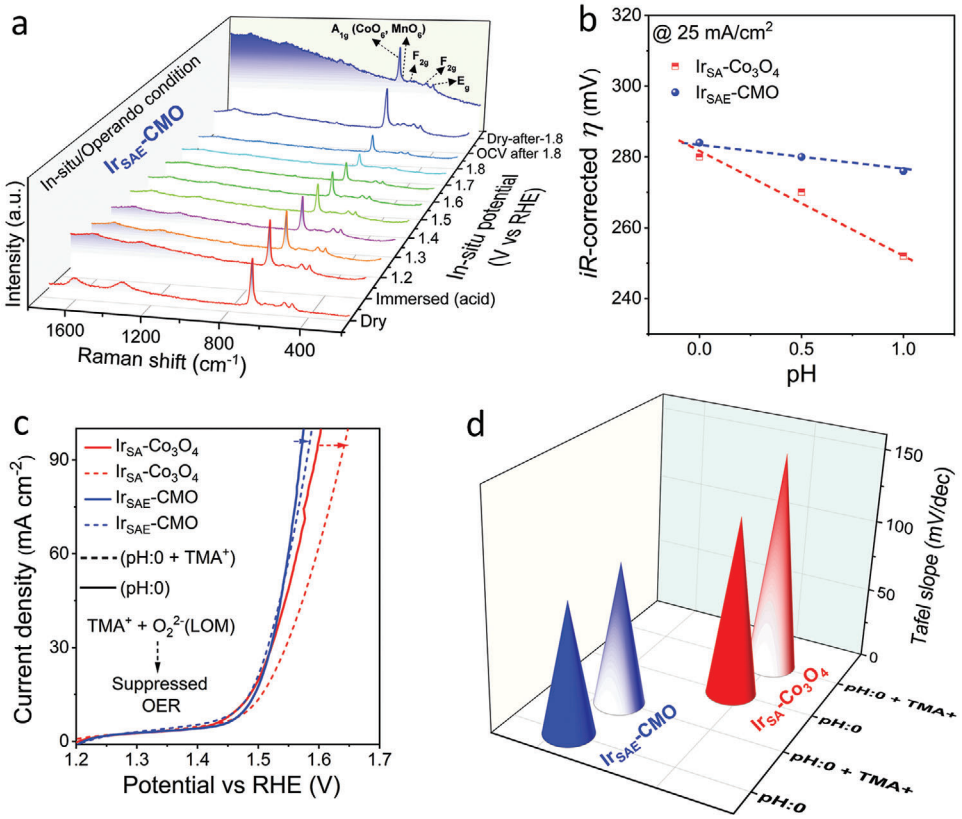

Figure 6. Operando Raman spectroscopy and catalytic mechanism. a) in situ Raman spectroscopy measurements for Ir_{SAE}-CMO recorded during acidic OER from 1.2 to 1.8 V vs RHE. All the characteristic bands originate from Mn-substituted Co_3O_4 spinel oxide and are well maintained during OER test. b) pH dependence of the OER potential at 25 mA cm^{-2} for Ir_{SAE}-CMO, and Ir_{SA}-Co_3O_4. c,d) OER LSV polarization curve of Ir_{SAE}-CMO, and Ir_{SA}-Co_3O_4 in 0.5 M H_2SO_4 (pH:0; solid line) and 0.5 M H_2SO_4 + 0.5 M $TMANO_3$ (pH:0 + TMA^+; dashed line) c), and corresponding Tafel slopes comparison in pH:0 and pH:0 + TMA^+ electrolyte d).

Figure S26a,b (Supporting Information), the Ir_{SA}-Co_3O_4 exhibited pronounced pH-dependent OER kinetics on the RHE scale, suggesting the involvement of lattice oxygen through the LOM pathway for OER.[29,33,34] Contrarily, the Ir_{SAE}-CMO showed negligible pH dependence OER kinetics on the RHE scale, providing evidence for the suppression of lattice oxygen participation during the OER process. To further verify the LOM pathway, peroxo-like O_2^{2-} chemical species generated during the LOM mechanism were tracked using tetramethylammonium cation (TMA^+), known for its specific interaction with negatively charged species on the catalyst surface and inhibit the LOM cascade.[32,33] The Ir_{SA}-Co_3O_4 displayed reduced OER activity and increased Tafel slopes in the presence of TMA^+, indicating the inhibition of the LOM pathway due to strong binding of TMA^+ (Figure 6c,d; Figure S26c, Supporting Information). In contrast, the OER kinetics of Ir_{SAE}-CMO remained largely unaffected in the presence of TMA^+, providing further confirmation that Ir_{SAE}-CMO effectively suppresses the lattice oxygen participation and does not follow the LOM pathway. Hence, with faster acidic OER kinetics (Tafel slope: 90 mV dec^{-1}), improved durability, and suppressed lattice oxygen participation, the Ir_{SAE}-CMO significantly outperformed the Ir_{SA}-Co_3O_4 (Tafel slope: 124 mV dec^{-1}). This superiority can be attributed to the rigid Ir_{SAE} structure's short and appropriate interatomic Ir-Ir distance which could facilitate direct oxo-oxo (O—O) radical coupling via oxide path mechanism (OPM) pathway, bypassing the need for additional *OOH intermediates (AEM), thus achieving superior acidic OER kinetics than Ir_{SA}-Co_3O_4 while maintaining excellent durability.

Additionally, operando X-ray absorption spectroscopy was used to further characterize the key intermediates of Ir_{SAE}-CMO under catalytic conditions applying a constant potential and simultaneously monitoring changes in the Ir L_3-edge features (**Figure** 7a; Figure S27a, Supporting Information). Analysis of the maximum edge position and the FT-EXAFS region at the open circuit potential (OCP) and at the OER thermodynamic potential (≈1.2 V vs RHE) indicated an overall oxidation state of +4, consistent with ex situ Ir L_3-edge experiments presented above (Figure 7b). Application of higher potential in the OER electrocatalytic region (≈1.45 V vs RHE) resulted in a significant shift of the edge to higher energies indicating the formation of species with a higher oxidation degree (Figure 7a,b). The correlation between the edge position and the oxidation state (O.S.) suggests the formation of a highly oxidized Ir (+5) intermediate.

The FT-EXAFS also showed notable differences before and during the catalytic process, which gave rise to a shorter peak in the FT-EXAFS spectrum at E_{app} 1.45 V vs RHE (Figure S27b, Supporting Information). In contrast to the spectra obtained at

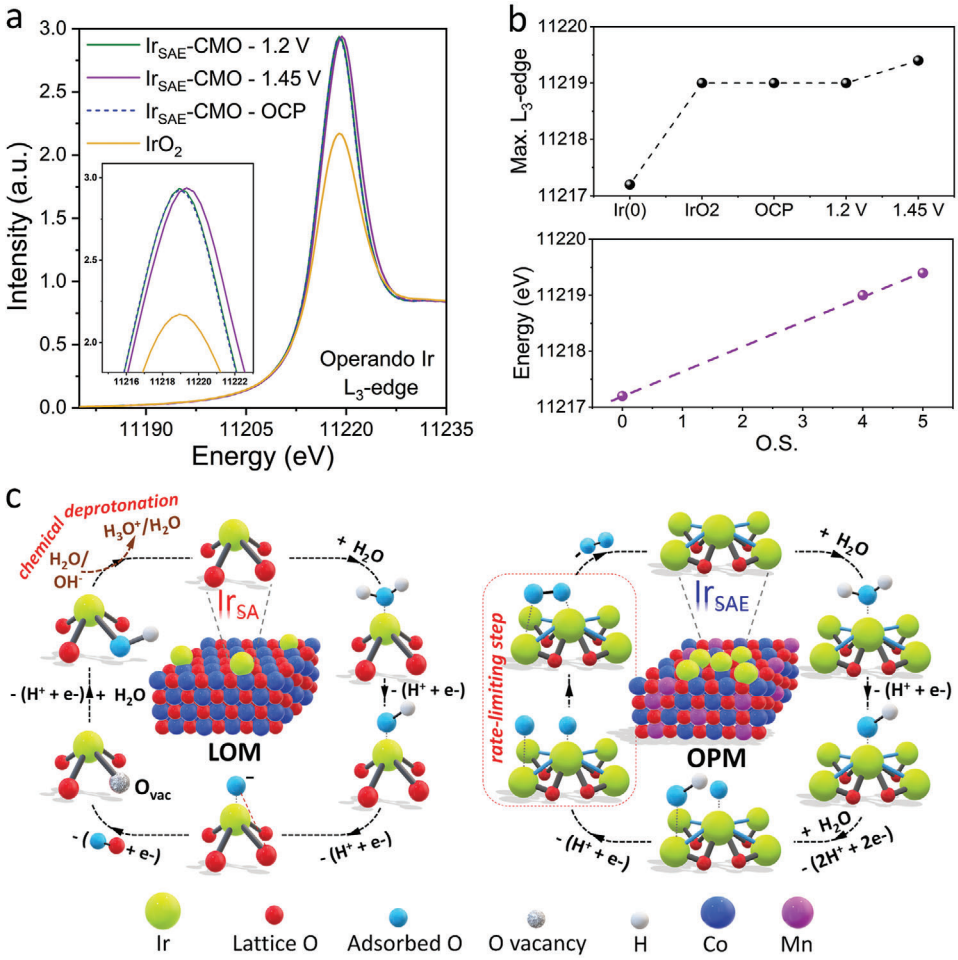

Figure 7. Operando X-ray absorption spectroscopy and mechanistic investigations. a) Experimental Ir-L_3 edge operando XANES spectra of Ir$_{SAE}$-CMO at OCP, 1.2 and 1.45 V vs RHE with IrO_2 reference sample. b) Positions of Ir-L_3 edge maximums at applied potentials (top) and their correlation with the iridium oxidation state (bottom). c) Proposed schematic illustration of lattice oxygen-mediated mechanism (LOM) process for Ir$_{SA}$-Co_3O_4 and oxide path mechanism (OPM) process for Ir$_{SAE}$-CMO.

OCP and OER thermodynamic potential, the first shell in the FT-EXAFS region could not be fitted using a simple Ir—O environment with a coordination number of 6 (Figures S27b, S28, S29 and Table S3, Supporting Information). The fitting of the experimental data significantly improved when for one of the paths the Ir—O distance was shortened, resulting in five Ir—O bonds at 2.0 Å and the shortened single Ir—O bond distance at 1.8 Å. This distance falls within the range expected for Ir^V = O moieties.[35] The detection of the Ir^V = O intermediate (typically namely Ir—O*) by operando XAS suggested that the kinetics of the OER reaction with Ir$_{SAE}$-CMO was limited by the O—O bond formation (rate-limiting step) and not the preceding electron transfer events. Finally, the energy profiles of each elementary steps during the OER via the AEM and OPM pathway on the Ir$_{SAE}$-CMO were calculated and compared (Figure S30, Supporting Information). The results indicate that the OPM pathway exhibits a lower energy barrier for the rate-determining step (1.81 eV; O*—O* coupling) compared to the AEM pathway (2.29 eV; formation of OOH*). This suggests that the short Ir–Ir interatomic distance within the Ir$_{SAE}$ facilitates direct O*—O* radical coupling via the OPM pathway, bypassing the need for additional OOH* intermediates, and leading to lower overall energy states.

Henceforth, the utilization of operando XAS measurements, in conjunction with the aforementioned analytical methodologies (pH-dependent activity test and molecular probe) and DFT calculations, clearly suggests that the Ir$_{SAE}$ with appropriate Ir—Ir interatomic distance significantly suppressed the lattice oxygen participation while facilitated direct oxo-oxo (O—O) radical coupling via the OPM pathway, thereby maintaining superior activity along with excellent stability in acidic OER. Accordingly, Figure 7c illustrates the proposed LOM pathway for Ir$_{SA}$-Co_3O_4 and the OPM pathway for Ir$_{SAE}$-CMO. The proposed LOM pathway for Ir$_{SA}$-Co_3O_4 triggers via the adsorption of a water molecule on the Ir$_{SA}$ site, followed by the removal of two protons and two electrons. Then the adsorbed-O on the Ir$_{SA}$ undergoes coupling with the lattice-O to generate molecular oxygen, while the water molecules from the electrolyte refill the generated oxygen vacancy, thereby completing the pathway. Whereas, in the proposed OPM pathway for Ir$_{SAE}$-CMO, two water molecules adsorbs on

the adjacent Ir sites of Ir_{SAE}, followed by the ejection of four protons and four electrons to generate two iridium-oxo (Ir—O*) sites in close vicinity. Then the two adsorbed-O in close proximity undergoes direct O—O radical coupling and gets released as molecular oxygen, thus completing the pathway and regenerating the active Ir_{SAE} site.

3. Conclusion

In summary, we demonstrated that spatially correlated Ir_{SAE} stabilized on the surface of Mn-substituted Co_3O_4 could achieve excellent mass activity and stability for acidic OER, attributed to the effective suppression of lattice oxygen participation and promotion of direct O—O radical coupling. DFT calculations further elucidated the role of Mn-substitution in the octahedral sites of Co_3O_4 in modulating surface binding energy and reducing migration energy barrier for Ir_{SA} on the CMO surface compared to Co_3O_4, facilitating the migration of Ir_{SA} to form short-range Ir_{SAE} structures. The detailed structural/electronic analysis of the Ir_{SAE}-CMO was performed using AC-HAADF STEM, XAS, and XPS, complemented by theoretical calculations, which elucidated the robust electronic interaction between rigid Ir_{SAE} and CMO support. Remarkably, the Ir_{SAE}-CMO exhibited outstanding mass activity and much-improved stability in acidic OER, surpassing both the benchmark IrO_2 and Ir_{SA}-Co_3O_4 catalysts. Furthermore, the negligible pH-dependent OER activity of Ir_{SAE}-CMO revealed the effective suppression of lattice oxygen participation, while the appropriate and short Ir—Ir distance in the Ir_{SAE} facilitated direct O-O radical coupling via oxide path mechanism, revealed by the operando Ir L_3-edge XAS analysis and DFT calculations. This leads to superior acidic OER kinetics while maintaining excellent durability. This study provides new insights for designing high-performance acidic OER catalysts for future proton exchange membrane water electrolyzers and other electrocatalysis applications.

4. Experimental Section

Chemicals: Cobalt(II) nitrate hexahydrate ($Co(NO_3)_2{\cdot}6H_2O$; Sigma–Aldrich, ≥99%), Manganese(II) nitrate tetrahydrate ($Mn(NO_3)_2{\cdot}4H_2O$; Sigma–Aldrich, ≥99%), Hexachloroiridium Acid Hydrate ($H_2IrCl_6{\cdot}xH_2O$; Sigma–Aldrich, ≥99.9%), Sodium sulfate (Na_2SO_4; Sigma–Aldrich, ≥99%), Tetramethylammonium nitrate ($(CH_3)_4N(NO_3)$; Sigma–Aldrich, ≥98%), Sulfuric acid (H_2SO_4; Sigma–Aldrich, ≥99.99%), nitric acid (HNO_3; Sigma–Aldrich, 70%), ethanol (C_2H_5OH; Sigma–Aldrich, ≥99.9%), Toray carbon cloth (CC, Alfa Aesar), and the nafion perfluorinated resin solution (5 wt %, Sigma–Aldrich) were used without further purification.

Synthesis of $Co_{3-x}Mn_x$ Hydroxide (x: 0/1) Precursors: In a typical procedure, a piece of CC was thoroughly washed in nitric acid, followed by rinsing and washing with deionized water and ethanol several times under ultrasonication. After completely drying the CC, the $Co_{3-x}Mn_x$ hydroxide (x: 0/1) precursors were electrodeposited on the CC at -1.1 V vs Ag/AgCl for 10 min in an aqueous solution containing an appropriate mixture of 0.1 M $Co(NO_3)_2{\cdot}6H_2O$ and 0.1 M $Mn(NO_3)_2{\cdot}4H_2O$ using a typical three-electrode electrochemical workstation. Then, the resultant samples were washed with DI water and ethanol, respectively, and dried at 60 °C overnight.

Synthesis of Co_3O_4 and CMO Supports: To obtain Co_3O_4 and CMO supports, the as-synthesized $Co_{3-x}Mn_x$-hydroxide (x: 0/1) was calcined at 350 °C for 3 h with a heating rate of 3 °C min^{-1}, followed by natural cooling to room temperature.

Synthesis of Ir_{SA}-Co_3O_4 and Ir_{SAE}-CMO: In a typical procedure, the Co_3O_4 and CMO supports were immersed in Ir-salt ethanolic solution (6 mg mL^{-1}) for 30 min, followed by drying in an oven. Then the samples were annealed in air at 350 °C for 2 h at a heating rate of 5 °C mi−^{1} (sample loading: 1 mg cm^{-2}) to obtain Ir_{SA}-Co_3O_4 and Ir_{SAE}-CMO. For control samples, Ir_{SA}-Co_3O_4 was also synthesized by varying the ethanol Ir-salt solution (3 and 10 mg mL^{-1}) denoted as Ir_{SA}-Co_3O_4-3 and Ir_{SA}-Co_3O_4-10.

Material Characterization: The crystal structures of all catalysts including their crystal orientations were measured by X-ray diffraction (XRD) operating in transmission mode at room temperature on a Stoe theta/theta diffractometer in Bragg-Brentano geometry with a Cu K$\alpha_{1,2}$ radiation X-ray source (λ: 1.5406 Å). FE-SEM images were obtained using a JEOL 7500F FE-SEM. The EDS patterns were collected using a Hitachi TM-3030 microscope equipped with a Si(Li) Pentafet plus detector from Oxford instruments. The ICP-OES measurement was carried out with a SPECTRO-GREEN instrument, and the electrolyte solution samples were taken from the electrochemical cell before and after the reaction. XPS analysis was performed with a VG ESCALAB 220i-XL with an X-ray source using monochromatic Al Kα anode (1486.6 eV) under the operation at 200 W and 15 kV. The base pressure in the analysis chamber during the experiment was 5×10^{-10} mbar. The C 1s peak for contaminant carbon was used as a reference at 284.5 eV for correction of the binding energy for surface charging. The aberration-corrected HAADF-STEM was obtained on a JEOL JEM ARM 200F instrument at 200 kV.

XAS Measurements—Ex situ Measurements: Co/Mn K-edge and Ir L_3-edge were used to measure Co_3O_4, CMO, Ir_{SA}-Co_3O_4 and Ir_{SAE}-CMO in fluorescence mode, and the reference samples Co(0), Mn_3O_4, MnO_4, Ir(0) and IrO_2 in transmission mode. Co/Mn K-edge and Ir L_3-edge were collected on BL10C beamline of the Pohang Light Source (PLS-II, Korea) and BL22 CLAESS at ALBA synchrotron (Spain), respectively. All powder samples were prepared by diluting the corresponding powder sample with cellulose in a pellet (φ = 6 mm). Afterward, the samples were placed in the sample holder and sealed with 30 µm Kapton tape. The Ir L_3-edge measurements, and the Mn K-edges of Mn_3O_4 and MnO_4 references were measured at BL10C (PLS-II synchrotron). The monochromatic X-ray beam was obtained using a liquid-nitrogen-cooled Si (111) double-crystal monochromator (Bruker ASC) from high-intensity X-ray photons of a multipole wiggler source. All X-ray absorption spectroscopic data were recorded in fluorescence mode using seven channels silicon drift detectors (SDD, Rayspec Ltd.) with high efficiency for extremely low concentration elements. Higher-order harmonic contaminations were eliminated by detuning to reduce the incident X-ray intensity by ≈30%. Energy calibration has been simultaneously carried out for each measurement with each reference metal placed in front of the third ion chamber. On the other hand, Co/Mn K-edges of Co_3O_4, CMO, Ir_{SA}-Co_3O_4, and Ir_{SAE}-CMO and Co(0) references were collected at BL22 CLAESS (ALBA synchrotron) using a Si (311) double crystal monochromator. The incident flux was ca. 5×10^{11} ph/sec. Incident energy was calibrated by assigning the inflection point of the corresponding metallic foil 6539 eV for Mn, 7709 eV for Co, and 11215 eV for the Ir. Final spectra were processed and normalized using Athena program, included in the DEMETER package.[36]

Operando X-ray Absorption Spectroscopy: Operando measurements were carried out to monitor the changes in the Ir L_3-edge for the Ir_{SAE}-CMO sample. The Ir L_3-edge XAS measurements were performed at the SAMBA beamline of the SOLEIL synchrotron, operated at an electron beam current of 450 mA. The incident energy was selected by a Si (200) double-crystal monochromator. Incident flux was ca. 1×10^{10} ph/sec using a beam size of 4 mm × 0.5 mm. Fluorescence spectra were recorded using a 36 elements germanium detector. The Ir_{SAE}-CMO electrodes were placed in a custom-built spectroelectrochemical (SEC) flow-cell and the SEC cell was attached to the sample stage using a custom-build plate designed to prevent and contain any electrolyte leaks. During the measurement, the electrolyte (0.5 M H_2SO_4) was continuously pumped through the cell (1.5–2.0 mL min^{-1}) using a membrane pump (Flow unit, Fluigent) controlled by a standalone vacuum pressure-based controller (Fluigent) to refresh

the solution and keep a constant pH. The pump worked in push mode using Ar. A SP-300 potentiostat (Biologic) was used to perform the CVs and CPE experiments during the measurements. In a typical experiment, two repetitive CV cycles were performed before applying the desired potential to conditionate the electrode and estimate the potential applied during the CPE. Afterward, controlled potential electrolysis was performed at the desired potentials (1.2 and 1.45 V vs RHE), and Ir L_3-edge XAS measurements were conducted simultaneously. Samples were measured at room temperature, and no signs of radiation-induced damage on the samples were observed during the measurements. The incident energy was calibrated by assigning the inflection point of an Ir foil to 11215 eV. Final spectra were processed and normalized using the Athena program, included in the DEMETER package.[36]

Electrochemical Measurements: The electrochemical tests were carried out using VSP-300 BioLogic potentiostat in a typical three-electrode configuration. The argon-purged 0.5 M H_2SO_4 was used as the electrolyte. As-prepared self-standing electrode was directly used as a working electrode (area: 0.7 × 0.6 cm^2), Ag/AgCl (3 M KCl) as the reference electrode, and Pt mesh as a counter electrode. The potential of the reference electrode was calibrated in H_2-saturated 0.5 M H_2SO_4 and all the potentials were converted to reversible hydrogen electrode (RHE) using the Nernst equation:

$$E_{(RHE)} = E_{(Ag/AgCl)} + E^0{}_{(Ag/AgCl)} + 0.059 \times pH \quad (1)$$

For fabricating the working electrode for commercial IrO_2, 5 mg of catalyst powder was dispersed in 500 µL of ethanol containing 20 µL 5% Nafion and sonicated for 60 min to get a homogeneous ink. Afterward, a certain quantity of the ink was drop-cast onto CC (loading: 1 mg cm^{-2}) and left to dry under ambient atmosphere. Before electrochemical measurements, the electrodes were saturated via cyclic voltammetry (CV) scans at a scan rate of 100 mV s^{-1} in argon-purge electrolyte. Linear sweep voltammetry (LSV) was taken at a slow scan rate of 5 mV s^{-1} to minimize the capacitive contribution. Nyquist plot were recorded using electrochemical impedance spectroscopy measurements in the faradaic region to estimate the solution resistance (R_s) charge transfer resistance (R_{CT}). Double-layer capacitance (C_{dl}) was obtained by collecting CVs at various scan rates of 10, 15, 20, 25, and 30 mV s^{-1} in the non-faradaic region. ECSA was obtained from the C_{dl} value using a specific capacitance of 0.06 mF cm^{-2}. The long-term durability test was performed with chronopotentiometry at a constant current density of 10 mA cm^{-2}.[37] To measure the metal leaching during the stability test, a small amount of the electrolyte was extracted from the cell after a certain time periods. To measure the faradaic efficiency, the actual amount of gas (oxygen) produced was measured using the water displacement method in an air-tight vessel.[7] All the potentials were iR-corrected with respect to the ohmic resistance of the solution obtained from the Nyquist plot unless specified:

$$E_{corrected} = E_{(RHE)} - iR \quad (2)$$

For pH-dependent study, a series of H_2SO_4 solutions were prepared with pH values of 0, 0.5, and 1. To maintain a constant ionic strength, an appropriated amount of Na_2SO_4 was added in the electrolyte.

In Situ/Operando Raman Spectroscopy Measurement: The in situ Raman measurements were carried out in a customized in situ electrochemical flow cell with an InVia Renishaw Raman microscope equipped with 532 nm of laser excitation wavelength, 1800 l mm^{-1} grading, and coupled with a 50x objective lens. The sample ink was drop-casted on the surface of rough Au foil and utilized as the working electrode, while Pt wire and Ag/AgCl were used as the counter and reference electrodes, respectively. 0.05 M H_2SO_4 (pH: 1) was used as the electrolyte. During the OER measurements, the electrolyte flow rate (5–8 mL min^{-1}) was controlled using a peristaltic pump. Ten consecutive scans with 10 s exposure time at 0.5 mW laser power were performed to measure in situ Raman spectra. The in situ Raman spectra were recorded using chronoamperometric mode with the potential held for 3 min from +1.2 V to 1.8 V vs RHE.

Computational Detail: All the DFT calculations were carried out using the Vienna ab initio simulation package (VASP) computational package,[38] a cutting-edge tool revered for its accuracy in simulating material properties at the quantum mechanical level. The exchange-correlation interactions, a central feature of DFT, are tackled using the Generalized Gradient Approximation (GGA) parameterized by Perdew, Becke, and Ernzerhof (PBE). This formulation is noted for its optimal balance of computational efficiency and physical realism, making it a preferred choice in the realm of DFT studies. Handling the interaction between core and valence electrons necessitates a precise yet efficient approach. For this purpose, the projector-augmented wave (PAW) technique,[39] a method renowned for accurately simulating the quantum states close to the atomic nucleus while retaining computational affordability was opted. These computations further involved the expansion of electronic wave-functions using plane waves. A cutoff energy of 400 eV for wave function expansion was set and used a k-point grid of (3 × 2 × 1) for Brillouin zone integration. This resolution was adequate to ensure numerical precision while controlling computational resources. To account for smearing effects, a Gaussian broadening of 0.05 eV was employed. To ensure the stability and reliability of computational results, all structures underwent relaxation under stringent convergence criteria. Specifically, a total energy difference of less than $1.0E^{-4}$ eV/atom and force less than 0.01 eV $Å^{-1}$ to consider the structure sufficiently relaxed was required. Additionally, a vacuum layer with a thickness of 15 Å along the *z* direction to avoid unwanted interactions between adjacent slab images in the periodic system was specified.[40] Beyond the structural and electronic properties, it delved into the dynamic behavior by investigating the energy barriers associated with ionic movement on the surface. The Climbing-Image Nudged Elastic Band method,[41] a state-of-the-art technique for identifying transition states, was employed for this purpose. Furthermore, Bader charge analysis was performed for all reactions, a method that provides a robust description of the charge density distribution in our system.

Supporting Information

Supporting Information is available from the Wiley Online Library or from the author.

Acknowledgements

H.T., A.K., Y.W., J.L., S.D., and O.R. thank the Max Planck Society (MPG) for basic funding. H.T. and S.D. thank the FUNCAT Centre of MPG. H.T. thanks the Bundesministerium für Bildung und Forschung (BMBF) of the German government for funding the Carbon2Chem project. This study was partly supported by the Volkswagen Foundation (96_742) and the Deutsche Forschungsgemeinschaft (DFG, German Research Foundation) Projektnummer 388390466–TRR 247 within the Collaborative Research Centre/Transregio 247 "Heterogeneous Oxidation Catalysis in the Liquid Phase". H.T. thanks the Spanish Ministry of Science, Innovation, and Universities for the ATRAE grant. The authors acknowledge Dr. Amol Jadhav for electron microscopy measurements. VQB thanks the Vietnam Ministry of Education and Training (code B2023.DNA.08). The authors also acknowledge Dr. Thi H. Ho for supporting the theoretical calculations. The authors acknowledge Dr. Claudia Weidenthaler and Sebastian Leiting for XPS measurements. The authors acknowledge Florian Baum for ICP-OES measurements. The authors also acknowledge the CLAESS beamline at the ALBA Synchrotron (proposal No. 2022086973), SAMBA beamline at the SOLEIL (proposal No. 20230111), and beamline staff for XAS measurements. JL acknowledges the support of the Marie Skłodowska-Curie grant No 101106576. MGS acknowledges the support of the HORIZON-MSCA-2021-PF project TRUSol No. 101063820. AK acknowledges the Alexander von Humboldt Foundation for a Humboldt Research Fellowship.

Open access funding enabled and organized by Projekt DEAL.

Conflict of Interest

The authors declare no conflict of interest.

Author Contributions

A.K. designed and carried out the experiments as well as analyzed the data with support from H.T., V.Q.B. performed the theoretical calculations. J.L. helped to conduct the EDS analysis. Y.W. helped in in situ Raman analysis. J.L. and Y.W. also helped in the data discussion. A.K., M.G.S., O.R., S.D., and MGK performed and analyzed ex situ and operando XAS measurements. A.K. and H.T. co-wrote the paper.

Data Availability Statement

The data that support the findings of this study are available from the corresponding author upon reasonable request.

Keywords

acidic water oxidation, hydrogen production, oxide-path mechanism, single-atom-ensembles, water splitting

Received: January 31, 2024
Revised: August 12, 2024
Published online: September 24, 2024

[1] M. Yu, E. Budiyanto, H. Tüysüz, *Angew. Chem., Int. Ed.* **2022**, *61*, 202103824.
[2] Z. Y. Wu, F. Y. Chen, B. Li, S. W. Yu, Y. Z. Finfrock, D. M. Meira, Q. Q. Yan, P. Zhu, M. X. Chen, T. W. Song, Z. Yin, H. W. Liang, S. Zhang, G. Wang, H. Wang, *Nat. Mater.* **2023**, *22*, 100.
[3] Y. Wen, P. Chen, L. Wang, S. Li, Z. Wang, J. Abed, X. Mao, Y. Min, C. T. Dinh, P. Luna, R. Huang, L. Zhang, L. Wang, L. Wang, R. J. Nielsen, H. Li, T. Zhuang, C. Ke, O. Voznyy, Y. Hu, Y. Li, W. A. Goddard, B. Zhang, H. Peng, E. H. Sargent, *J. Am. Chem. Soc.* **2021**, *143*, 6482.
[4] X. Liu, S. Xi, H. Kim, A. Kumar, J. Lee, J. Wang, N. Q. Tran, T. Yang, X. Shao, M. Liang, M. G. Kim, H. Lee, *Nat. Commun.* **2021**, *12*, 5676.
[5] H. Tüysüz, *Acc. Chem. Res.* **2024**, *57*, 558.
[6] M. Yu, C. Weidenthaler, Y. Wang, E. Budiyanto, E. Onur Sahin, M. Chen, S. DeBeer, O. Rudiger, H. Tüysüz, *Angew. Chem., Int. Ed.* **2022**, *61*, 202211543.
[7] A. Kumar, S. Bhattacharyya, *ACS Appl. Mater. Interfaces* **2017**, *9*, 41906.
[8] A. Kumar, D. K. Chaudhary, S. Parvin, S. Bhattacharyya, *J. Mater. Chem. A.* **2018**, *6*, 18948.
[9] X. Chen, J. Liu, T. Yuan, Z. Zhang, C. Song, S. Yang, X. Gao, N. Wang, L. Cui, *Energy Mater* **2022**, *2*, 200028.
[10] Y. Q. Zhang, B. Ouyang, J. Xu, G. C. Jia, S. Chen, R. S. Rawat, H. J. Fan, *Angew. Chem., Int. Ed.* **2016**, *55*, 8670.
[11] L. An, C. Wei, M. Lu, H. W. Liu, Y. B. Chen, G. G. Scherer, A. C. Fisher, P. X. Xi, Z. C. J. Xu, C. H. Yan, *Adv. Mater.* **2021**, *33*, 2006328.
[12] J. Lee, A. Kumar, T. Yang, X. H. Liu, A. R. Jadhav, G. H. Park, Y. Hwang, J. M. Yu, C. T. K. Nguyen, Y. Liu, S. Ajmal, M. G. Kim, H. Lee, *Energy Environ. Sci.* **2020**, *13*, 5152.
[13] A. Zagalskaya, V. Alexandrov, *ACS Catal.* **2020**, *10*, 3650.
[14] S. Geiger, O. Kasian, M. Ledendecker, E. Pizzutilo, A. M. Mingers, W. T. Fu, O. Diaz-Morales, Z. Z. Li, T. Oellers, L. Fruchter, A. Ludwig, K. J. Mayrhofer, M. T. M. Koper, S. Cherevko, *Nat. Catal.* **2018**, *1*, 508.
[15] Y. Pi, Q. Shao, P. Wang, J. Guo, X. Huang, *Adv. Funct. Mater.* **2017**, *27*, 1700886.
[16] G. H. Moon, Y. Wang, S. Kim, E. Budiyanto, H. Tüysüz, *ChemSusChem* **2022**, *15*, 202102114.
[17] S. Chen, H. Huang, P. Jiang, K. Yang, J. F. Diao, S. P. Gong, S. Liu, M. X. Huang, H. Wang, Q. W. Chen, *ACS Catal.* **2020**, *10*, 1152.
[18] C. Lin, J. L. Li, X. P. Li, S. Yang, W. Luo, Y. J. Zhang, S. H. Kim, D. H. Kim, S. S. Shinde, Y. F. Li, Z. P. Liu, Z. Jiang, J. H. Lee, *Nat. Catal.* **2021**, *4*, 1012.
[19] Y. Li, Y. Wang, J. Lu, B. Yang, X. San, Z.-S. Wu, *Nano Energy* **2020**, *78*, 105185.
[20] A. Kumar, V. Q. Bui, J. Lee, L. L. Wang, A. R. Jadhav, X. H. Liu, X. D. Shao, Y. Liu, J. M. Yu, Y. Hwang, H. T. D. Bui, S. Ajmal, M. G. Kim, S. G. Kim, G. S. Park, Y. Kawazoe, H. Lee, *Nat. Commun.* **2021**, *12*, 6766.
[21] A. Kumar, X. H. Liu, J. Lee, B. Debnath, A. R. Jadhav, X. D. Shao, V. Q. Bui, Y. Hwang, Y. Liu, M. G. Kim, H. Lee, *Energy Environ. Sci.* **2021**, *14*, 6494.
[22] X. Li, W. Xu, Y. Fang, R. Hu, J. Yu, H. Liu, W. Zhou, *SusMat* **2023**, *3*, 160.
[23] J. Q. Shan, C. Ye, S. M. Chen, T. L. Sun, Y. Jiao, L. M. Liu, C. Z. Zhu, L. Song, Y. Han, M. Jaroniec, Y. H. Zhu, Y. Zheng, S. Z. Qiao, *J. Am. Chem. Soc.* **2021**, *143*, 5201.
[24] M. Zlatar, D. Nater, D. Escalera-Lopez, R. M. Joy, P. Pobedinskas, K. Haenen, C. Coperet, S. Cherevko, *Electrochim. Acta* **2023**, *444*, 141982.
[25] A. Kumar, V. Q. Bui, J. Lee, A. R. Jadhav, Y. Hwang, M. G. Kim, Y. Kawazoe, H. Lee, *ACS Energy Lett.* **2021**, *6*, 354.
[26] A. Kumar, J. Lee, M. G. Kim, B. Debnath, X. H. Liu, Y. Hwang, Y. Wang, X. D. Shao, A. R. Jadhav, Y. Liu, H. Tüysüz, H. Lee, *ACS Nano* **2022**, *16*, 15297.
[27] A. Kumar, S. Parvin, R. K. Das, S. Bhattacharyya, *Chem Asian J* **2021**, *16*, 3444.
[28] E. Budiyanto, S. Salamon, Y. Wang, H. Wende, H. Tüysüz, *JACS Au* **2022**, *2*, 697.
[29] A. Grimaud, A. Demortière, M. Saubanère, W. Dachraoui, M. Duchamp, M. L. Doublet, J. M. Tarascon, *Nat. Energy* **2017**, *2*, 16189.
[30] A. Grimaud, O. Diaz-Morales, B. H. Han, W. T. Hong, Y. L. Lee, L. Giordano, K. A. Stoerzinger, M. T. M. Koper, Y. Shao-Horn, *Nat. Chem.* **2017**, *9*, 457.
[31] P. Garrido-Barros, C. Gimbert-Suriñach, R. Matheu, X. Sala, A. Llobet, *Chem. Soc. Rev.* **2017**, *46*, 6088.
[32] Z. F. Huang, S. B. Xi, J. J. Song, S. Dou, X. G. Li, Y. H. Du, C. Z. Diao, Z. C. J. Xu, X. Wang, *Nat. Commun.* **2021**, *12*, 3992.
[33] A. K. Tomar, U. N. Pan, N. H. Kim, J. H. Lee, *ACS Energy Lett.* **2022**, *8*, 565.
[34] Y. N. Wang, M. C. Zhang, Z. Y. Kang, L. Shi, Y. C. Shen, B. Y. Tian, Y. C. Zou, H. Chen, X. X. Zou, *Nat. Commun.* **2023**, *14*, 5119.
[35] R. S. Hay-Motherwell, G. Wilkinson, B. Hussain-Bates, M. B. Hursthouse, *Polyhedron* **1993**, *12*, 2009.
[36] B. Ravel, M. Newville, *J. Synchrotron Radiat.* **2005**, *12*, 537.
[37] M. Yu, G. H. Moon, R. G. Castillo, S. DeBeer, C. Weidenthaler, H. Tüysüz, *Angew. Chem., Int. Ed.* **2020**, *59*, 16544.
[38] V. Q. Bui, A. Kumar, H. T. Bui, J. Lee, Y. Hwang, H. M. Le, Y. Kawazoe, H. Lee, *Chem. Mater.* **2020**, *32*, 9591.
[39] Y. Liu, L. Wang, L. Chen, H. Wang, A. R. Jadhav, T. Yang, Y. Wang, J. Zhang, A. Kumar, J. Lee, V. Q. Bui, M. G. Kim, H. Lee, *Angew. Chem., Int. Ed.* **2022**, *61*, 202209555.
[40] H. T. Bui, V. Q. Bui, X. D. Shao, A. Kumar, S. G. Kim, H. M. Le, Y. Kawazoe, H. Lee, *J. Phys. Chem. C* **2021**, *125*, 13176.
[41] G. Henkelman, B. P. Uberuaga, H. Jónsson, *J. Chem. Phys.* **2000**, *113*, 9901.